

Article

## Geometric Characteristics of Three Dimensional Reconstructed Anode Electrodes of Lithium Ion Batteries

Cheolwoong Lim <sup>1</sup>, Bo Yan <sup>1,2</sup>, Leilei Yin <sup>3</sup> and Likun Zhu <sup>1,\*</sup>

<sup>1</sup> Department of Mechanical Engineering, Indiana University-Purdue University Indianapolis, Indianapolis, IN 46202, USA; E-Mail: cheolmail@gmail.com

<sup>2</sup> School of Materials Science and Engineering, Shanghai Jiao Tong University, Shanghai 200030, China; E-Mail: luxer@sjtu.edu.cn

<sup>3</sup> Beckman Institute, University of Illinois, Urbana, IL 61801, USA; E-Mail: yin@illinois.edu

\* Author to whom correspondence should be addressed; E-Mail: likzhu@iupui.edu; Tel.: +1-317-274-4887; Fax: +1-317-274-9744.

Received: 25 February 2014; in revised form: 31 March 2014 / Accepted: 1 April 2014 /

Published: 22 April 2014

---

**Abstract:** The realistic three dimensional (3D) microstructure of lithium ion battery (LIB) electrode plays a key role in studying the effects of inhomogeneous microstructures on the performance of LIBs. However, the complexity of realistic microstructures imposes a significant computational cost on numerical simulation of large size samples. In this work, we used tomographic data obtained for a commercial LIB graphite electrode to evaluate the geometric characteristics of the reconstructed electrode microstructure. Based on the analysis of geometric properties, such as porosity, specific surface area, tortuosity, and pore size distribution, a representative volume element (RVE) that retains the geometric characteristics of the electrode material was obtained for further numerical studies. In this work, X-ray micro-computed tomography (CT) with 0.56  $\mu\text{m}$  resolution was employed to capture the inhomogeneous porous microstructures of LIB anode electrodes. The Sigmoid transform function was employed to convert the initial raw tomographic images to binary images. Moreover, geometric characteristics of an anode electrode after 2400 cycles at the charge/discharge rate of 1 C were compared with those of a new anode electrode to investigate morphological change of the electrode. In general, the cycled electrode shows larger porosity, smaller tortuosity, and similar specific surface area compared to the new electrode.

**Keywords:** lithium ion batteries (LIBs); computed tomography (CT); geometric characteristics; representative volume element (RVE)

---

## 1. Introduction

Rechargeable lithium ion batteries (LIBs) have shown excellent potential as power sources for electric vehicles [1]. Recently LIBs have already been employed in pure electric cars such as the Nissan Leaf and Chevrolet Spark EV. However, obstacles still lie in the way of widely deploying LIBs in electric vehicles. For instance, the energy density of LIBs is not high enough to support a long-distance commute. The cost of LIB packs in electric vehicles is still high. The battery pack for the Nissan Leaf costs about \$12,000 [2]. Fire, explosion, and gas ruptures caused by unpredicted catastrophic failures are still big safety concerns [3–5]. To successfully implement LIBs in electric vehicles, further improvements for LIB technologies are required. In addition to the development of advanced materials for the anode, cathode, and electrolyte [6], the structure of the electrodes at the micro- and nano-scales also plays a critical role in determining the performance of a LIB because the electrode's composite matrix must be designed to provide both electron and lithium ion transportation, which eventually affects the LIB's voltage, specific capacity, and discharge/charge rate.

In the past several years, numerical studies have been conducted to investigate the morphological effects on the performance of LIBs. For instance, Wang *et al.* [6] found that the microstructure of the LIB electrode significantly affects achievable capacity by comparing the numerical results of the randomly and regularly packed electrode structures. Goldin *et al.* [7] showed that the packing configuration of particles affects lithium ion transport, thereby affecting the performance of LIBs. Smith *et al.* [8] developed a two dimensional (2D) ion transport model using scanning electron microscope (SEM) images of LIB electrodes. They showed that the local inhomogeneity of the electrode microstructure causes localized lithium depletion and leads to an increase in the polarization losses of the anode. These numerical studies elucidated the effects of the electrode's microstructure on battery performance. However, the 2D model and the assumed microstructure do not represent the real complex morphology of LIB electrodes. The realistic three dimensional (3D) microstructure of LIB electrodes is required to perform this study [9].

Recently, tomographic technologies have been used to obtain the real configuration of LIB electrode microstructures. For instance, focused ion beam SEM (FIB-SEM) has been used to reconstruct the 3D microstructure of LIB electrodes [10–12]. X-ray computed tomography (CT) is another technique that enables the reconstruction of the 3D morphology of LIB electrodes [13–15]. With the tunable X-ray energy available at the synchrotron sources, X-ray nano-tomography has been successfully applied to reveal elemental information in the composite electrodes for both LIBs and solid oxide fuel cells [16–18]. The reconstructed morphologies have been utilized to study geometric characteristics and their effects on lithium ion transport. For example, Shearing *et al.* [15] revealed the spatial distribution of tortuosity, specific surface area, and porosity in a graphite negative electrode of a commercial LIB. Kehward *et al.* [19] demonstrated geometric inhomogeneity effects on tortuosity of a reconstructed microstructure which could not be predicted by the Bruggeman relation.

Furthermore, numerical studies were performed directly using the 3D reconstructed electrodes to characterize the performance of LIBs. For instance, Weidemann *et al.* [20] developed a computational model that resolves the complex 3D microstructure of LIB cathodes and showed the local variations of lithium ion concentration and electrostatic potential in realistic electrodes. In our previous studies, the 3D numerical simulation also revealed the non-uniform spatial distributions of the potential, concentration, intercalation reaction rate, heat generation rate, and stress development [21–23]. The realistic microstructure of LIB electrodes play a key role to study morphological effects on lithium ion transport, electrochemical kinetics, material degradation, and cell performance.

However, the complexity of realistic microstructures imposes a significant computational cost on numerical simulation of large size samples. A representative volume element (RVE) that retains the geometric characteristics of an inhomogeneous electrode material allows minimizing the volume of the porous microstructure generated by tomography techniques for further numerical studies. Kehrwald *et al.* [19] and Izzo *et al.* [24] investigated the change of porosity and tortuosity by increasing the size of sub-samples for a bulk porous microstructure to identify the size of RVE. In their studies, the tortuosity fluctuated until the size reached the entire volume while the porosity was stabilized at a certain size. The purpose of this paper is to investigate the geometric characteristics of inhomogeneous anode electrodes of a commercial LIB and describe a method to find the RVE of a reconstructed 3D LIB electrode based on the analysis of geometric characteristics. In this study, we investigated the geometric characteristics of reconstructed LIB anode electrodes. In addition, the geometric parameters of a cycled electrode were compared with those of a new electrode to demonstrate changes of the parameters after a large number of cycles. X-ray micro-CT was employed to capture the inhomogeneous porous microstructures of the electrodes. After obtaining the binary data of the CT images, the geometric properties were computed using the binary data of a reconstructed 3D geometry. The geometric properties including porosity, pore size distribution, specific surface area, and tortuosity, were accounted to find a RVE of the electrode for further numerical studies.

## 2. Experimental

### 2.1. Sample Preparation

A commercial LIB with 40 mA·h capacity (SP035518AB, Tianjin Lishen Battery Co., Tianjin, China) was cycled to obtain an aged anode electrode. It was charged/discharged from 2.8 V to 4.2 V at 1 C (40 mA) current rate under galvanostatic condition. The anode of the LIB is mesocarbon microbeads (MCMB) graphite (92 wt% MCMB and 8 wt% polyvinylidene fluoride (PVDF) binder) and the cathode is lithium cobalt oxide (94 wt% LiCoO<sub>2</sub>, 3 wt% carbon black, and 3 wt% PVDF binder). After 2400 cycles, the capacity of the LIB decreased more than 10% of the initial capacity. In this study, a new anode electrode and the aged anode electrode were scanned to perform the structural analysis. An Xradia microXCT-400 system (Xradia, Pleasanton, CA, USA) was employed to obtain the CT images of the electrodes. A total of 729 projection images were captured over 182 degrees scan angle. The spatial resolution of the CT had been set as 0.56 μm. To enhance the brightness and contrast of the whole dataset, X-ray measurement parameters were optimized for different samples. For the new anode electrode, the X-ray source was set at 60 kV and 8 W and each projection exposure time was 30 s.

For the cycled anode electrode, the X-ray source was set at 25 kV and 5 W and each projection exposure time was 25 s. Detailed information about sample preparation can be found in our previous publication [23].

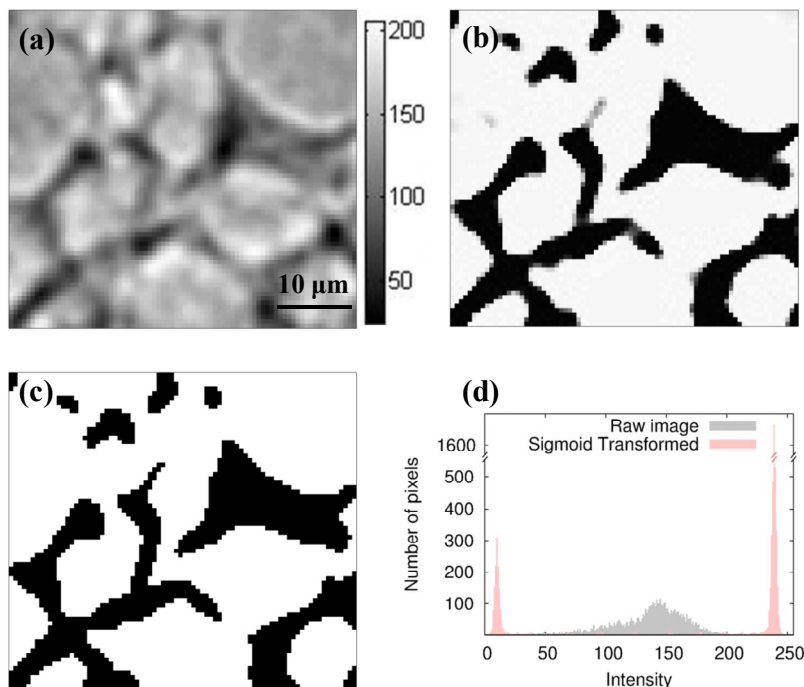
## 2.2. Segmentation

To reconstruct the 3D porous microstructure of the anode electrode, the raw data set generated by micro-CT needs to be converted to binary data, which is completely divided in material and pore phases. The pixel values in the raw images indicate the X-ray absorption rate that depends on the material at the given position. The intensity values of pixels in a 2D sample image are shown as a grayscale image in Figure 1a. Bright color regions with high intensity values represent the graphite particles, while the rest of the image is regarded as the pore phase of the anode electrode. The anode electrode also includes 8 wt% PVDF binder and its main functionality is to bind graphite particles and anode current collector together. In LIB electrodes, PVDF binder usually forms porous structure with thin layers for lithium ion transport [25]. Due to the low X-ray absorption of the porous binder and its irregular shape, the PVDF binder phase cannot be distinguished from the pore phase by the Xradia microXCT-400 system. In this study, the pore phase contains both pores and PVDF binder. The size of the sample image is  $44.8 \times 39.2 \mu\text{m}^2$  that corresponds to  $80 \times 70$  pixels. To generate a binary matrix from a raw data set, a simple threshold method could be applied on the raw data by a local minimum of the intensity histogram [26,27]. As shown in Figure 1d, since the intensity profile of the sample image does not have a clear phase boundary between pores and anode materials, it is difficult to define a threshold value directly from the raw image. Manual segmentation based on experiences is often time consuming, expensive, and non-reproducible. For this reason, an image segmentation technique were employed to enhance the edge contrast and generate the binary data using the Insight Toolkit (ITK) [28]. The image segmentation method is described using the sample image shown in Figure 1a. First, the raw image was filtered by the ITK curvature anisotropic diffusion filter to remove noise effects and enhance the interface between two different phases. Second, the intensity values of the filtered image were transformed based on the Sigmoid function. The function is given by:

$$I' = (I_{\max} - I_{\min}) \cdot \frac{1}{1 + e^{-\frac{I-\beta}{\alpha}}} + I_{\min} \quad (1)$$

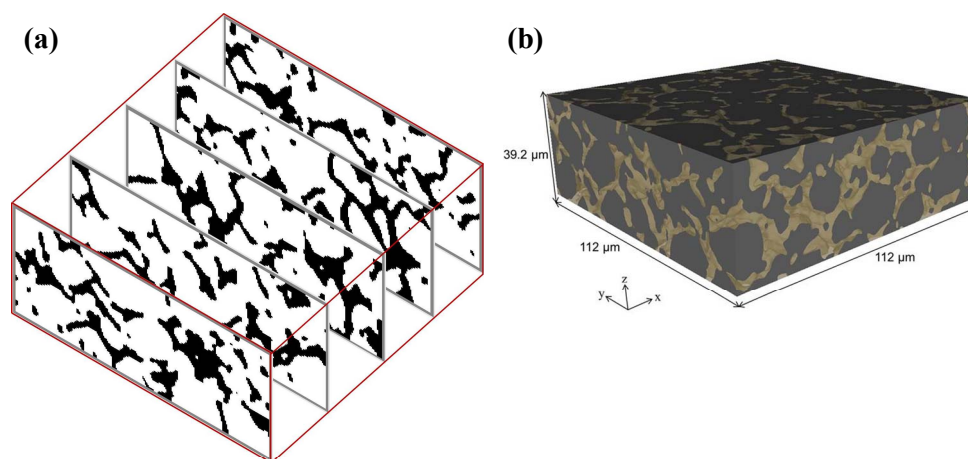
where  $I$  is the intensity of the input pixel;  $I'$  is the intensity of the output pixel;  $I_{\min}$  and  $I_{\max}$  are the minimum and maximum values of the output image;  $\alpha$  is the width of the input intensity range; and  $\beta$  is the centered intensity of the range. This method has been applied as an intensity transformation to enhance low contrast images [29,30]. The variables ( $\alpha = 10$ ,  $\beta = 124$ ) were iteratively obtained to generate a smooth and continuous boundary of the image. In Figure 1b, a Sigmoid transformed image clearly shows the porous structure of the sample image. A threshold intensity value can be selected from the transformed histogram in Figure 1d to distinguish the graphite phase and the pore phase. Finally, the binary matrix (Figure 1c) was obtained by performing the simple threshold method using the threshold defined in the previous step.

**Figure 1.** Image processing to generate a binary matrix: (a) a raw image of the new anode electrode from X-ray micro-computed tomography (CT); (b) the sigmoid transformed image of (a); (c) the binary image of (b); and (d) intensity histogram of the raw image and Sigmoid transformed image.



After segmentation, a set of binary images were stacked with a  $0.56 \mu\text{m}$  interval to reconstruct the porous microstructure. Figure 2a shows the aligned images of a domain with  $200 \times 200 \times 70$  voxels in 3D. An interface surface between graphite and pore phases was calculated by creating polygons based on the aligned binary data. The Visualization Toolkit (VTK) [31] with ITK was employed to extract the interface from the binary data. Figure 2b shows a reconstructed microstructure with an entire volume of  $112 \times 112 \times 39.2 \mu\text{m}^3$ . The graphite geometry is indicated in gray color and the pore structure is indicated in yellow color. The volume fraction of pores over the bulk domain is 0.27 with 99% of pore connectivity.

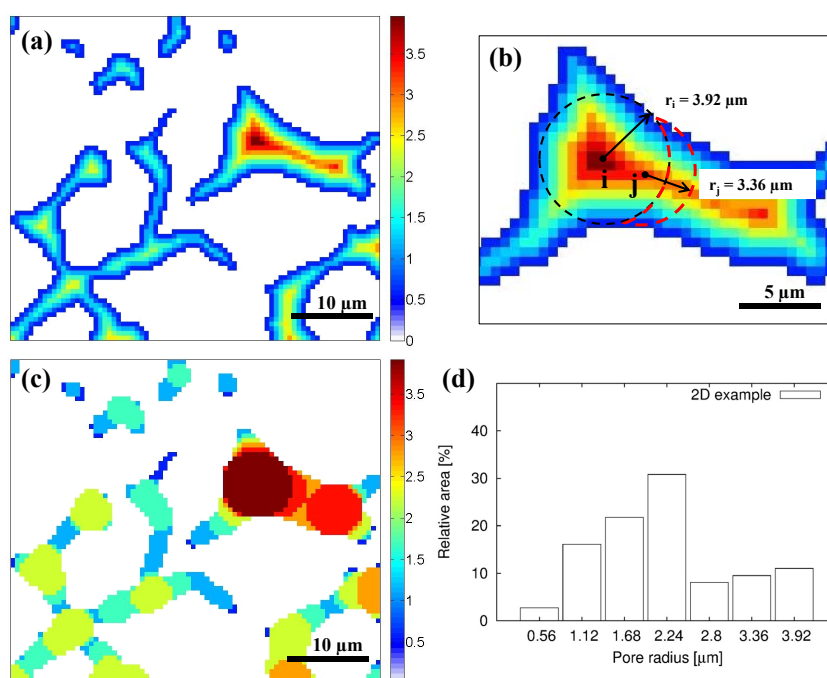
**Figure 2.** Reconstruction of an anode electrode: (a) aligned three dimensional (3D) binary matrix; and (b) a reconstructed microstructure of the anode electrode.



### 2.3. Quantification of Geometric Characteristics

Geometric parameters, such as porosity, tortuosity, specific surface area, and pore size distribution are important factors affecting the capacity, reaction kinetics, and lithium ion transport of LIBs. Porosity is a fraction of the pore volume over the total electrode volume and was directly calculated from the binary matrix. Specific surface area is the solid-electrolyte interface area of an electrode per bulk volume and was calculated after reconstructing the microstructure from the binary matrix. Tortuosity quantifies the sinuosity and interconnectedness of the electrolyte phase to predict lithium ion transport in the porous electrode. The approach in [19] was employed to obtain the tortuosity data. An approach similar to the one shown in [32] was employed to obtain the pore size distribution for the anode geometry. As a first step, Euclidean distance from the interface to all voxel points in the pore phase was calculated using the binary matrix. The Danielsson distance map module of the ITK was employed to obtain the distance map of the binary matrix. The pore size distributions of real samples shown in this paper were calculated in 3D. Volume, voxel, and inscribed sphere were used. To clearly explain the approach to obtain pore size distribution, a 2D image was used as an example. Figure 3a shows a 2D distance map through the Danielsson distance map module of the ITK. All pixel values represent the distance from the surface of the white colored anode material. The pore size of any pixel was set to be the radius of the largest inscribed circle that covers the pixel. For example, pixel  $i$  and  $j$  in Figure 3b have the same pore size of  $3.92 \mu\text{m}$ . Figure 3c shows the pore size map from the distance map of the sample binary matrix. To quantify the result, Figure 3d shows a histogram that represents the area fraction of pore sizes for the 2D sample image. The smallest pore size corresponds with the spatial resolution of the X-ray projection ( $0.56 \mu\text{m}$ ). The pore size distribution enables to describe inhomogeneous characteristics of the electrode material which is not predicted by porosity.

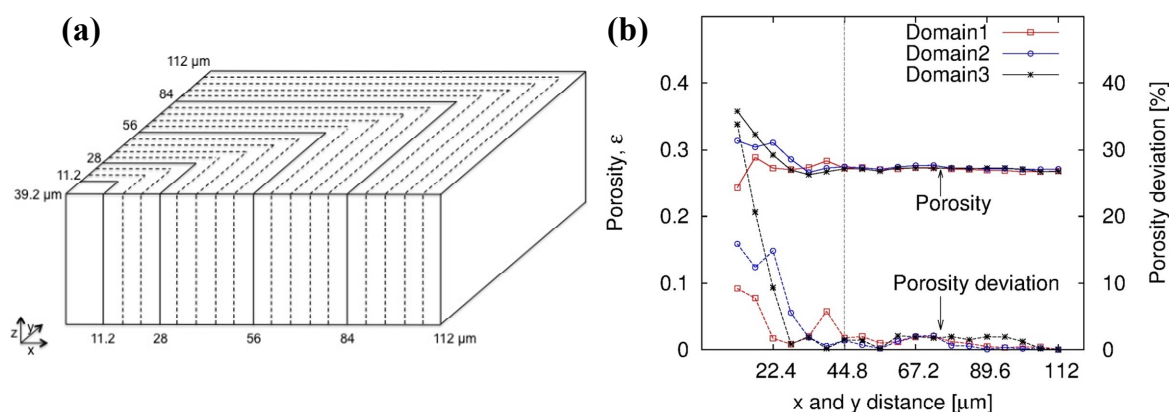
**Figure 3.** (a) Euclidean distance map from the interface between material (white region) and pore (colored region) phases; (b) the selected Region A of the distance map; (c) pore radii of the distance map; and (d) pore size distribution of the sample image.



### 3. Results and Discussion

Three domains with the same size ( $112 \times 112 \times 39.2 \mu\text{m}^3$ ) were captured from the binary data of a new anode material to determine the optimal size of the RVE. Sub-divisions of each domain were obtained by increasing  $x$  and  $y$  lengths from the initial volume ( $11.8 \times 11.8 \times 39.2 \mu\text{m}^3$ ) to investigate the influence of the volume on porosity. The thickness ( $z$ -axis) was fixed for all sub-divisions and it is the thickness of the anode electrode. Figure 4b shows the change of porosity of the domains with the volume change (Figure 4a). The porosity of the domains is around 0.27. The porosity of the sub-divisions tends to converge to the porosity of the domain by increasing the volume. For all domains, the deviation of the porosity of sub-divisions remains within 2% of the domain porosity when the lengths of  $x$  and  $y$  directions are longer than  $44.8 \mu\text{m}$ . Based on this result, the size of the RVE was chosen as  $44.8 \times 44.8 \times 39.2 \mu\text{m}^3$ .

**Figure 4.** (a) Subdivisions of the new electrode domains are captured by increasing  $x$  and  $y$  lengths with fixed thickness ( $39.2 \mu\text{m}$  in  $z$  direction); and (b) the porosity profile of the Domain 1. Dash lines represent the porosity deviation.



Adapting the size, we collected 16 sample candidates from Domain 1, which have porosities within 2% deviation from the porosity of Domain 1. 3D surfaces of the 16 samples were reconstructed to obtain specific surface area. As shown in Figure 5a, the specific surface areas of the samples are around  $0.24$ – $0.27 \mu\text{m}^{-1}$  and the specific surface area of Domain 1 is  $0.25$ . The maximum deviation from the specific surface area of Domain 1 is 6.26%. 10 samples have the specific surface areas within 2% deviation from the specific surface area of Domain 1. Figure 5b shows the tortuosity of the Domain 1 and the 16 samples. Most of the samples tend to have higher tortuosity than Domain 1. This result is very similar with the tortuosity results shown in [19]. It is because we assume the four boundaries along  $x$  and  $y$  directions of samples are impermeable. The smaller samples tend to have longer average diffusion path ways throughout  $z$  direction due to the impermeable boundaries. As shown in [15], the tortuosity of the samples would converge to the domain value when the size of the samples reached around the size of the domain. The results in Figure 5b also show large deviations from the tortuosity of Domain 1 (2.11). The tortuosity of the 16 samples is from 2.01 to 2.53, and the maximum deviation from the tortuosity of Domain 1 is 19.88%. Figure 5b shows four samples (samples number are 4, 8, 12, and 14) in the range of 2% of tortuosity deviation from Domain 1. The pore size distribution quantifies the inhomogeneity of the complex 3D morphology of the samples. It could be an important

geometric parameter to define a RVE for the domain. Pore size distributions of the domain and its sub-samples were obtained from a 3D distance map of the microstructures.

**Figure 5.** (a) Specific surface areas; and (b) tortuosities of the sample microstructures are shown with the value of Domain 1 for the new anode electrode. The red line indicates the specific surface area or tortuosity of Domain 1 and the gray region indicates the 2% deviation of the domain value.

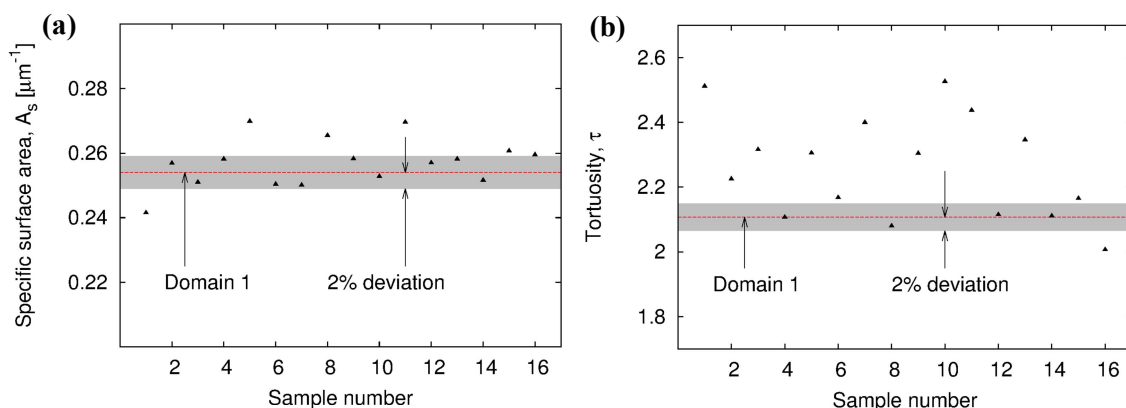
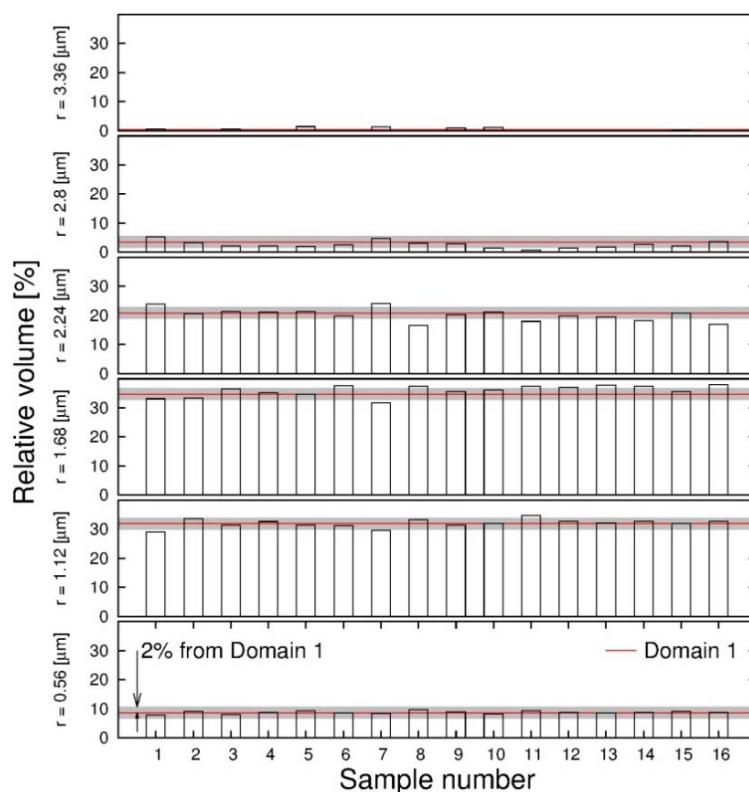


Figure 6 shows the pore size distribution and the obtained pore sizes were ranged from 0.56  $\mu\text{m}$  to 3.36  $\mu\text{m}$ . The pore size distributions tend to have larger deviation at larger pore sizes.

**Figure 6.** Pore size distributions of the sample microstructures of Domain 1 for the new anode electrode are shown as relative volume fraction of the pore phase. The red lines are the values for Domain 1 and the gray regions indicate the 2% difference from the domain values for each pore size.



The average absolute deviations from the pore size distribution of Domain 1 are shown in Table 1. At  $r = 3.36 \mu\text{m}$ , only six samples have this pore size. In this study, we only considered pore sizes between  $0.56 \mu\text{m}$  to  $2.8 \mu\text{m}$  for determining RVEs because the relative volume at  $3.36 \mu\text{m}$  is less than 2%. As shown in Figure 6, the gray colored regions represent the volume fraction at the size with 2% difference from the domain values. Five samples (samples number are 2–5 and 9) have pore size distribution within 2% difference of the domain value.

**Table 1.** Average absolute deviations of the pore size distribution of sub-samples from the domain value for the new and cycled anode electrode.

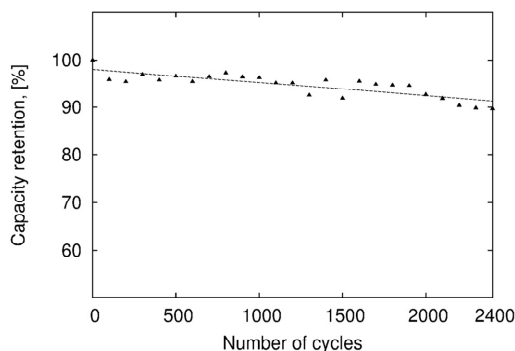
Pore size ( $\mu\text{m}$ )		0.56	1.12	1.68	2.24	2.8	3.36	3.92	4.48
Average absolute deviation	New	4.56%	3.26%	5.57%	7.59%	36.69%	131.33%	-	-
	Cycled	8.54%	5.56%	5.56%	9.35%	17.84%	29.67%	89.84%	184.06%

With the quantified geometric characteristics shown in Figures 4–6, a method was utilized to find a RVE that retains the geometric characteristics of the original inhomogeneous electrode geometry. First, the optimal size of the RVE was determined by investigating the convergence of porosity of sub-samples for a bulk porous microstructure. The size of RVE for the new anode electrode was determined to be  $44.8 \times 44.8 \times 39.2 \mu\text{m}^3$ , because the porosity fluctuation of the sub-divisions converged to within 2% of the porosity of the domain. Second, 16 samples were collected from Domain 1. The size of samples is  $44.8 \times 44.8 \times 39.2 \mu\text{m}^3$ , and the porosity of the samples is within 2% deviation of the porosity of the domain. Third, the RVE candidates were filtered by selecting samples within 2% deviation of the domain's specific surface area and tortuosity. Three RVE candidates (samples number are 4, 12, and 14) were selected. Finally, the three RVE candidates were filtered by the pore size distribution. Since the pore size distribution has much larger deviation from the domain value, we chose 2% difference from the domain value as the threshold. After filtering, Sample 4 maintained the geometric characteristics such as porosity, pore size distribution, specific surface, and tortuosity of Domain 1 and it can be selected as the RVE for further numerical studies.

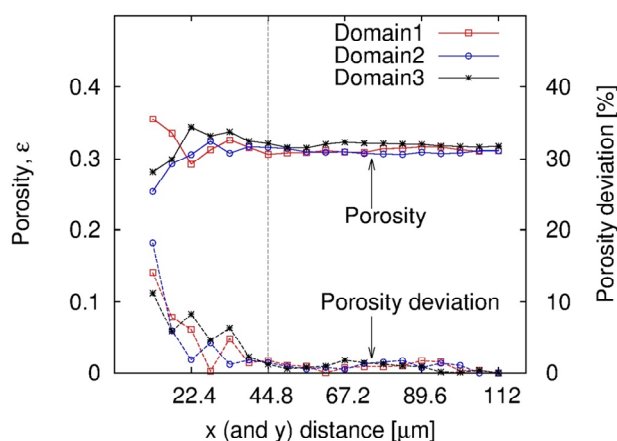
In order to investigate the geometric change of the LIB anode electrode after a large number of discharge and charge cycles, a commercial LIB was discharged/charged at 1 C current rate under galvanostatic conditions for 2400 cycles. As shown in Figure 7, it retains about 90% of the initial capacity after cycling. X-ray micro-CT generated images of the cycled anode electrode were employed to examine the geometric characteristics of the anode material. First, three domains ( $112 \times 112 \times 39.2 \mu\text{m}^3$ ) were selected to decide the size of the RVE from the binary data. As shown in Figure 8, the porosity profile converges to the domain's porosity by increasing the volume. The size of the RVE was determined to be  $44.8 \times 44.8 \times 39.2 \mu\text{m}^3$  same as the new electrode. For the cycled electrode, 15 samples were collected as RVE candidates with 2% porosity deviation from Domain 2 ( $\varepsilon = 0.31$ ). Figure 9a shows that the specific surface areas of the samples are around  $0.23\text{--}0.27 \mu\text{m}^{-1}$  and the specific surface area of Domain 2 is 0.26, which is similar to the new electrode. The maximum deviation from the specific area of Domain 2 is 8.46%. Five samples have specific surface areas within the 2% deviation from the specific surface area of Domain 2. Figure 9b shows the tortuosity of Domain 2 and the 15 samples ranging from 1.72 to 2.14. The maximum deviation from the tortuosity of Domain 2 is 14.97%.

Figure 9b shows two samples (samples number are 3 and 14) are in the range of 2% of tortuosity deviation from Domain 2. The pore sizes were evaluated using the binary data of the samples.

**Figure 7.** Discharge capacity of the commercial lithium ion battery (LIB) by the number of discharge and charge cycles.



**Figure 8.** Porosity profiles of the domains for the cycled anode electrode by increasing  $x$  and  $y$  lengths with fixed thickness ( $39.2 \mu\text{m}$  in  $z$  direction). Dash lines represent the porosity deviation.



**Figure 9.** (a) Specific surface areas; and (b) tortuosities of the sample microstructures are shown with the value of Domain 2 for the cycled anode electrode. The red line indicates specific surface area or tortuosity of Domain 2 and the gray region indicates the 2% deviation of the domain value.

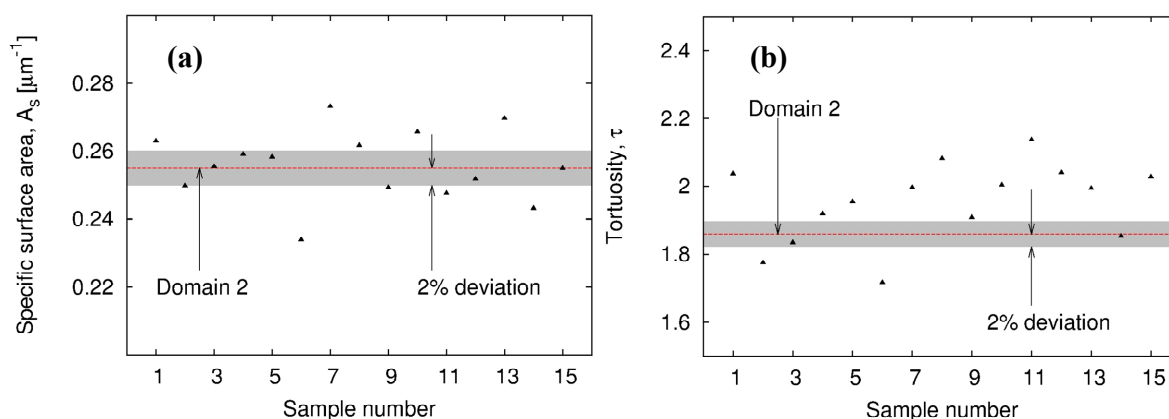
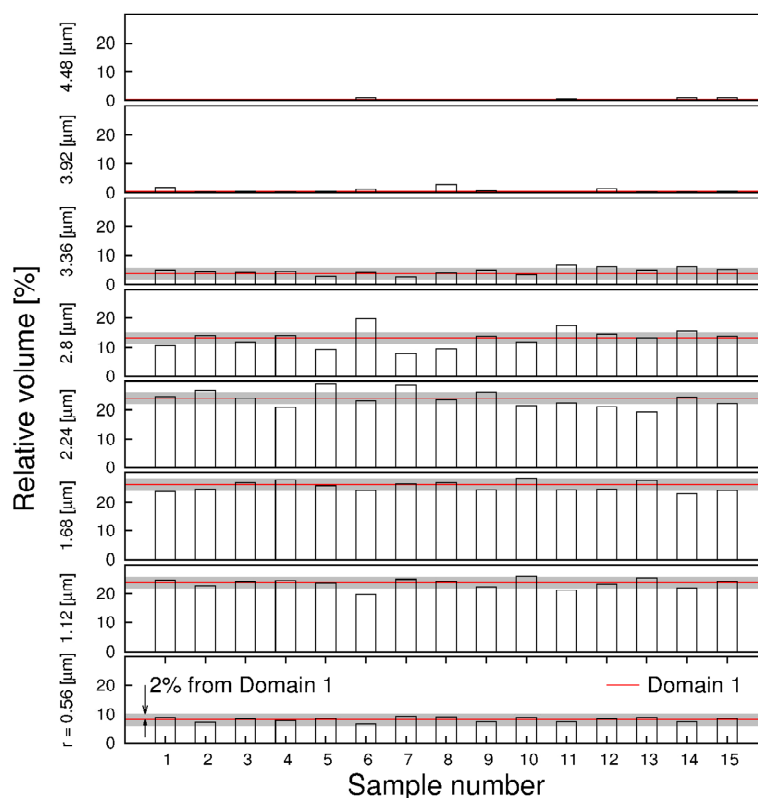


Figure 10 shows the pore size distribution and the obtained pore sizes were from 0.56  $\mu\text{m}$  to 4.48  $\mu\text{m}$ . The average absolute deviations from the pore size distribution of Domain 2 are shown in Table 1. At  $r = 4.48 \mu\text{m}$ , only four samples have this pore size. The gray colored regions present the volume fraction at the pore size with the 2% difference from the domain values. Three samples (samples number are 3, 9, and 15) have pore size distributions within the 2% difference of the domain value. By choosing the same filtering thresholds as the new electrode, Sample 3 was the only RVE which can maintain geometric properties of the original geometry.

**Figure 10.** Pore size distributions of the sample microstructures of Domain 2. The gray regions indicate the 2% difference from the domain values (red lines).



In this study, the geometric characteristics of the cycled anode microstructure were investigated and a RVE was determined based on the structural analysis. The geometric properties of the new and cycled anode material are summarized in Table 2.

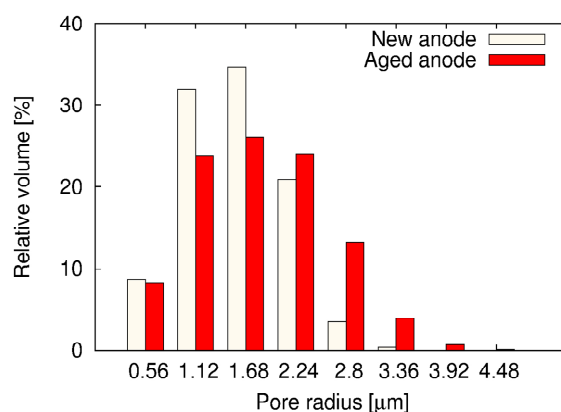
**Table 2.** Quantitative geometric parameters of the new anode material and the cycled anode material.

Electrode	Porosity, $\epsilon$	Specific surface area, $A_s$ ( $1/\mu\text{m}$ )	Tortuosity, $\tau$
New anode	0.27	0.25	2.11
Cycled anode	0.31	0.26	1.86

Figure 11 shows the pore size distribution of the new and cycled electrodes. The porosity results show that the cycled LIB lost about 5.6% active material in anode electrode. The specific surface area of the cycled anode geometry is similar with that of the new anode geometry. The specific surface area

between the active material and the liquid electrolyte is not affected by the porosity change because the pore size distribution of the cycled electrode was also changed. Figure 11 shows that the cycled electrode has more large pores compared to the new electrode. Larger pores can result in smaller specific surface area. According to the tortuosity and pore size distribution, we can expect that lithium ion transport in the cycled cell is easier than in the new cell. However, Figure 7 shows 10% capacity loss. The structure change of the anode electrode cannot explain the capacity loss by itself. For example, solid electrolyte interphase (SEI) layer on the electrode could reduce accessible surface area for lithium ions even if the specific surface area was very similar with the initial status [33]. There could also be another possible reason for the capacity fade [34]. As shown in [20], the capacity of a LIB was dominated by the cathode material rather than the anode material. The SEI layer formation during cycling could cause the loss of lithium ions in the electrolyte and increase the resistance of intercalation reaction at the interface of active material and electrolyte. In summary, there are many possible reasons for the capacity losses which we cannot directly deduce from our morphology analysis.

**Figure 11.** Pore size distributions of the new anode material and the cycled anode material.



#### 4. Conclusions

In this work, realistic microstructures were generated to characterize the geometric properties of the anode electrode material by employing X-ray micro-CT technology on a commercial LIB. The binary data which represents graphite and pore phases were obtained from the grayscale CT images by applying the Sigmoid transform function in an open-source, cross-platform system—IJK. Geometric properties of the anode microstructures, such as porosity, pore size distribution, specific surface area, and tortuosity are inhomogeneous. Based on the quantified geometric properties, a RVE retaining the geometric characteristics of the original geometry was determined for further numerical studies. Also, the geometric properties between a new electrode and a cycled electrode were compared. The cycled anode electrode shows larger porosity, smaller tortuosity, and similar specific surface area. The cycled electrode includes more large pores compared to the new electrode.

#### Acknowledgments

The authors would like to thank Tianjin Lishen Battery Joint-Stock Co. for providing lithium ion batteries. Acknowledgment is made to the donors of The American Chemical Society Petroleum Research Fund for support of this research.

## Author Contributions

Cheolwoong Lim contributed to the numerical simulation and structural analysis. Leilei Yin carried out the experiments on micro-CT scan of LIB electrodes. All the authors contributed to the data analysis, discussion of the results, and writing the manuscript at all stages.

## Conflicts of Interest

The authors declare no conflict of interest.

## References

1. Vetter, J.; Novák, P.; Wagner, M.R.; Veit, C.; Möller, K.C.; Besenhard, J.O.; Winter, M.; Wohlfahrt-Mehrens, M.; Vogler, C.; Hammouche, A. Ageing mechanisms in lithium-ion batteries. *J. Power Sources* **2005**, *147*, 269–281.
2. Bullis, K. How improved batteries will make electric vehicles competitive? *Technol. Rev.* **2013**, *116*, 19–20.
3. Zhang, J.L.; Lee, J. A review on prognostics and health monitoring of Li-ion battery. *J. Power Sources* **2011**, *196*, 6007–6014.
4. Orendorff, C.J.; Roth, E.P.; Nagasubramanian, G. Experimental triggers for internal short circuits in lithium-ion cells. *J. Power Sources* **2011**, *196*, 6554–6558.
5. Yoon, W.S.; Nam, K.W.; Jang, D.; Chung, K.Y.; Hanson, J.; Chen, J.M.; Yang, X.Q. Structural study of the coating effect on the thermal stability of charged mgo-coated  $\text{LiNi}_{0.8}\text{Co}_{0.2}\text{O}_{0.2}$  cathodes investigated by *in situ* XRD. *J. Power Sources* **2012**, *217*, 128–134.
6. Wang, C.-W.; Sastry, A.M. Mesoscale modeling of a Li-ion polymer cell. *J. Electrochem. Soc.* **2007**, *154*, A1035–A1047.
7. Goldin, G.M.; Colclasure, A.M.; Wiedemann, A.H.; Kee, R.J. Three-dimensional particle-resolved models of Li-ion batteries to assist the evaluation of empirical parameters in one-dimensional models. *Electrochim. Acta* **2012**, *64*, 118–129.
8. Smith, M.; Garcia, R.E.; Horn, Q.C. The effect of microstructure on the galvanostatic discharge of graphite anode electrodes in  $\text{LiCoO}_2$ -based rocking-chair rechargeable batteries. *J. Electrochem. Soc.* **2009**, *156*, A896–A904.
9. Thiedmann, R.; Stenzel, O.; Spetl, A.; Shearing, P.R.; Harris, S.J.; Brandon, N.P.; Schmidt, V. Stochastic simulation model for the 3D morphology of composite materials in Li-ion batteries. *Comput. Mater. Sci.* **2011**, *50*, 3365–3376.
10. Wilson, J.R.; Cronin, J.S.; Barnett, S.A.; Harris, S.J. Measurement of three-dimensional microstructure in a  $\text{LiCoO}_2$  positive electrode. *J. Power Sources* **2011**, *196*, 3443–3447.
11. Hutzenlaub, T.; Thiele, S.; Zengerle, R.; Ziegler, C. Three-dimensional reconstruction of a  $\text{LiCoO}_2$  Li-ion battery cathode. *Electrochem. Solid-State Lett.* **2012**, *15*, A33–A36.
12. Ender, M.; Joos, J.; Carraro, T.; Ivers-Tiffée, E. Three-dimensional reconstruction of a composite cathode for lithium-ion cells. *Electrochem. Commun.* **2011**, *13*, 166–168.
13. Ebner, M.; Geldmacher, F.; Marone, F.; Stampanoni, M.; Wood, V. X-ray tomography of porous, transition metal oxide based lithium ion battery electrodes. *Adv. Energy Mater.* **2013**, *3*, 845–850.

14. Yufit, V.; Shearing, P.; Hamilton, R.W.; Lee, P.D.; Wu, M.; Brandon, N.P. Investigation of lithium-ion polymer battery cell failure using X-ray computed tomography. *Electrochem. Commun.* **2011**, *13*, 608–610.
15. Shearing, P.R.; Howard, L.E.; Jørgensen, P.S.; Brandon, N.P.; Harris, S.J. Characterization of the 3-dimensional microstructure of a graphite negative electrode from a Li-ion battery. *Electrochem. Commun.* **2010**, *12*, 374–377.
16. Chen-Wiegart, Y.C.K.; Cronin, J.S.; Yuan, Q.X.; Yakal-Kremski, K.J.; Barnett, S.A.; Wang, J. 3D non-destructive morphological analysis of a solid oxide fuel cell anode using full-field X-ray nano-tomography. *J. Power Sources* **2012**, *218*, 348–351.
17. Chen-Wiegart, Y.C.K.; DeMike, R.; Erdonmez, C.; Thornton, K.; Barnett, S.A.; Wang, J. Tortuosity characterization of 3D microstructure at nano-scale for energy storage and conversion materials. *J. Power Sources* **2014**, *249*, 349–356.
18. Chen-Wiegart, Y.C.K.; Liu, Z.; Faber, K.T.; Barnett, S.A.; Wang, J. 3D analysis of a  $\text{LiCoO}_2\text{-Li}(\text{Ni}_{1/3}\text{Mn}_{1/3}\text{Co}_{1/3})\text{O}_2$  Li-ion battery positive electrode using X-ray nano-tomography. *Electrochem. Commun.* **2013**, *28*, 127–130.
19. Kehrwald, D.; Shearing, P.R.; Brandon, N.P.; Sinha, P.K.; Harris, S.J. Local tortuosity inhomogeneities in a lithium battery composite electrode. *J. Electrochem. Soc.* **2011**, *158*, A1393–A1399.
20. Wiedemann, A.H.; Goldin, G.M.; Barnett, S.A.; Zhu, H.; Kee, R.J. Effects of three-dimensional cathode microstructure on the performance of lithium-ion battery cathodes. *Electrochim. Acta* **2013**, *88*, 580–588.
21. Yan, B.; Lim, C.; Yin, L.L.; Zhu, L.K. Three dimensional simulation of galvanostatic discharge of  $\text{LiCoO}_2$  cathode based on X-ray nano-CT images. *J. Electrochem. Soc.* **2012**, *159*, A1604–A1614.
22. Yan, B.; Lim, C.; Yin, L.; Zhu, L. Simulation of heat generation in a reconstructed  $\text{LiCoO}_2$  cathode during galvanostatic discharge. *Electrochim. Acta* **2013**, *100*, 171–179.
23. Lim, C.; Yan, B.; Yin, L.; Zhu, L. Simulation of diffusion-induced stress using reconstructed electrodes particle structures generated by micro/nano-CT. *Electrochim. Acta* **2012**, *75*, 279–287.
24. Izzo, J.R.; Joshi, A.S.; Grew, K.N.; Chiu, W.K.S.; Tkachuk, A.; Wang, S.H.; Yun, W.B. Nondestructive reconstruction and analysis of SOFC anodes using X-ray computed tomography at sub-50 nm resolution. *J. Electrochem. Soc.* **2008**, *155*, B504–B508.
25. Yoshio, M.; Brodd, R.J.; Kozawa, A. *Lithium-ion Batteries: Science and Technologies*; Springer: New York, NY, USA, 2009.
26. Joos, J.; Carraro, T.; Weber, A.; Ivers-Tiffée, E. Reconstruction of porous electrodes by FIB/SEM for detailed microstructure modeling. *J. Power Sources* **2011**, *196*, 7302–7307.
27. Münch, B.; Holzer, L. Contradicting geometrical concepts in pore size analysis attained with electron microscopy and mercury intrusion. *J. Am. Ceram. Soc.* **2008**, *91*, 4059–4067.
28. Ibanez, L.; Schroeder, W.; Ng, L.; Cates, J. *The ITK Software Guide*, 2nd ed.; Kitware Inc.: Clifton Park, NY, USA, 2005.
29. Hassan, N.Y.; Aakamatsu, N. Contrast enhancement technique of dark blurred image. *IJCSNS Int. J. Comput. Sci. Netw. Secur.* **2006**, *6*, 223–226.
30. Hertz, J. *Introduction to the Theory of Neural Computation*; Basic Books: New York, NY, USA, 1991; Volume 1.

31. Schroeder, W.; Martin, K.; Lorensen, B. *The Visualization Toolkit*, 2nd ed.; Prentice Hall PTR: Upper Saddle River, NJ, USA, 1998.
32. Thiele, S.; Zengerle, R.; Ziegler, C. Nano-morphology of a polymer electrolyte fuel cell catalyst layer—Imaging, reconstruction and analysis. *Nano Res.* **2011**, *4*, 849–860.
33. Broussely, M.; Herreyre, S.; Biensan, P.; Kasztejna, P.; Nechev, K.; Staniewicz, R.J. Aging mechanism in Li ion cells and calendar life predictions. *J. Power Sources* **2001**, *97–98*, 13–21.
34. Amatucci, G.G.; Tarascon, J.M.; Klein, L.C. Cobalt dissolution in LiCoO<sub>2</sub>-based non-aqueous rechargeable batteries. *Solid State Ion.* **1996**, *83*, 167–173.

© 2014 by the authors; licensee MDPI, Basel, Switzerland. This article is an open access article distributed under the terms and conditions of the Creative Commons Attribution license (<http://creativecommons.org/licenses/by/3.0/>).